ADVANCED FUNCTIONAL MATERIALS
www.afm-journal.de

Materials Views
www.MaterialsViews.com

Effect of Nano-Porosity on High Gain Permeable Metal-Base Transistors

*Hyeonggeun Yu, Jong H. Kim, Wenchao Chen, Doyoung Kim, Jing Guo, and Franky So**

As one type of vertical thin-film transistors, permeable metal-base transistors (PMBTs) with a permeable metal film embedded between two semiconductor layers have been proposed for high gain current amplifier. In principle, compared with conventional bipolar transistors, PMBTs should have a higher speed and are easier to fabricate compatible with flexible and printed electronics. However, functional PMBTs are not realized due to low current gains (<50) and lack of output current saturation. In this paper, making use of the nano-textured surface of an organic semiconductor, we are able to fabricate devices with permeable metal base films having a pore size of about 20 nm and achieve current gains up to 476 with output current saturation. Correlations between the nano-scale porosity and the charge transmission/amplification behaviors in the device are explained with characterization of the metal base porosity. From our device simulation results, the small pore size is essential to achieve current saturation in the device due to the potential-pinning effect in the small pore regions. Finally, using a similar strategy, we also demonstrate a high gain (=260) solution-processed metal oxide-based PMBTs with output current saturation.

1. Introduction

A permeable metal base transistor (PMBT) is a vertical thin-film transistor that has a permeable metal film embedded between two semiconductor layers that function as an emitter and a collector in the device. Various techniques have been used to fabricate a permeable metal base, and they include deposition of a porous conducting polymer thin film,[1,2] deposition of an ultra-thin metal film,[3–5] and patterning a mesh electrode by colloidal lithography.[6,7] PMBTs are similar to conventional bipolar junction transistors (BJTs) given the fact that the emitter-collector current is controlled by the base current, unlike a field-effect transistor that controls the source-drain current by the gate voltage. Accordingly, the principal function of a PMBT is a current amplifier rather than a voltage-controlled driving transistor used in logic circuits.

H. Yu, Dr. J. H. Kim, Dr. D. Y. Kim, Prof. F. So
Department of Materials Science and Engineering
University of Florida
Gainesville, FL 32611–6400, USA
E-mail: fso@mse.ufl.edu
W. Chen, Prof. J. Guo
Department of Electrical and Computer Engineering
University of Florida
P.O. Box 116130, Gainesville, FL 32611–6130, USA

DOI: 10.1002/adfm.201400634

Compared with BJTs, PMBTs have a different device operation mechanism. PMBTs are considered as Schottky back-to-back diodes, and the majority carrier drift currents through the permeable metal base regions are the dominant charge transmission mechanism in active mode. In BJTs, on the other hand, minority carrier diffusion current from the emitter layer into the base layer is required for charge transmission in the device. As a result, the origin of the base current (or input current) in PMBTs is the charge carriers flowing from the emitter layer into the non-permeable metal base regions, whereas, in BJTs, recombination of the minority carriers in the base layer gives rise to the base current. With the developments of high mobility organic materials and low temperature film deposition techniques, PMBTs are gaining advantages over BJTs, such as a simple device structure, low temperature, solution processibility compatible with flexible and printed electronics, and potentially higher device speed due to the low base resistance.[8]

Current gain (β) in PMBT is defined by the ratio of the change in collector current (output current) to the change in base current (input current). To function as a power amplifier, a high current gain with output current saturation is required. Excellent current saturation characteristics are indispensable to achieve a large unitary power gain frequency. Additionally, the collector current in the saturation region should be a linear function of the base current, or in other words, the current gain defined in the saturation region must be constant for different base currents. The best way to characterize a true current amplification factor in PMBTs is to measure the common-emitter characteristics. In the common-emitter measurement configuration, output collector current versus emitter-collector voltage (V_{CE}) are measured under a fixed base current.

However, high-performance PMBTs have not been realized due to low current gains and non-saturated output currents. In fact, most of high gain PMBTs reported in the literature cannot be realized for the following reasons. First, it is commonly assumed that a high common-base gain ($\alpha = I_C/I_E$) measured would lead to a high common-emitter gain ($\beta = I_C/I_E$) based on the relation of $\beta = \alpha/(1-\alpha)$. As a result, only the common-base characteristics were demonstrated.[9–12] However, a high α value does not necessarily lead to the calculated high β value in the common-emitter measurement. Unless the high β is realized in a collector current saturation region in a common-emitter plot,

it is not sufficient to conclude that this transistor can yield a high current gain. Second, extremely high current gains up to 4,000 have been reported using an organic emitter and n-Si collector employing a thin metal film as the base.[13–15] However, collector current saturation was not demonstrated in this type of devices, and the high β value defined in the non-saturated collector current region is not meaningful for use as a practical analog amplifier. Third, high current gains up to 150 have been reported under base voltage-controlled common-emitter configuration.[16–18] Unlike typical common-emitter configuration that fixes the base current, in this configuration, the emitter-collector voltage was swept under a fixed base voltage, treating the device like a voltage controlled transistor instead of a current amplifier. Although collector current saturation was observed from the measurement, no linear relationship was found between the base current (input) and the collector current (output). As a result, the current gains were not consistent for different base voltages, which is not suitable for current amplifier applications.

Recently, several reports have demonstrated collector current saturation in base current-controlled common-emitter configuration by employing a thin metal film as the base, but the current gains were all less than 50.[19–24] The low gains were mainly due to the difficulty in controlling the nano-scale porosity in the thin metal base films. Additionally, correlation between the natural porosity and the device performance has never been examined systematically, limiting understanding of the underlying physics in PMBTs.

In this work, we demonstrate high gain organic n-type PMBTs by use of C_{60} as the emitter, Al thin film as the base, and N,N′-dimethyl-3,4,9,10-perylene tetracarboxylic diimide (Me-PTCDI) as the collector. Because of the granular structure on the Me-PTCDI surface, we found that the nano-porosity of the metal base can be controlled by tuning the nominal thickness of the metal base film. As a result, high current gains up to 476 were achieved with output current saturation in base current-controlled common-emitter configuration. The nano-porosity was calculated using atomic force microscopy (AFM) images and the voltage feedback analysis. Based on our device simulation results, the pore size is more important for current saturation than pore density since the potential-pinning effect within the pore becomes more significant with smaller pore size. To yield a high current gain with current saturation, we discovered that a pore size of 20 nm is required. Based on the understanding of the device physics, we also demonstrated a NiO-based p-type PMBT with saturated current gain of 260 under base current-controlled common-emitter configuration.

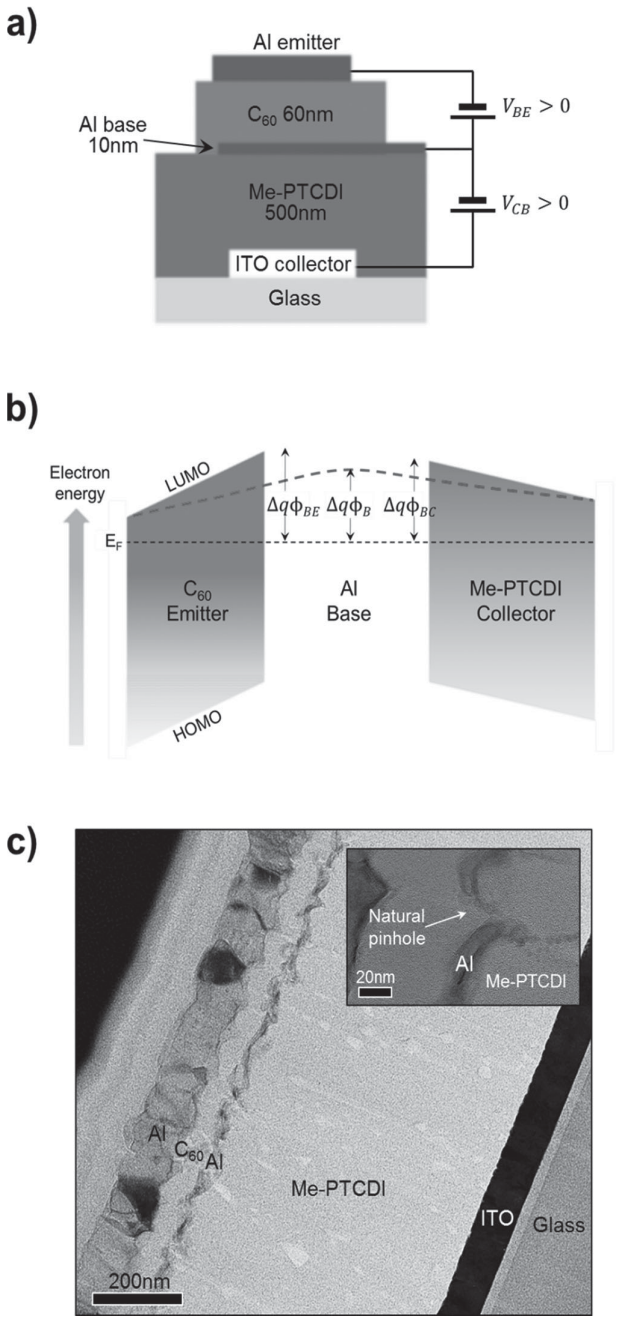

Figure 1. (a) Schematic device structure and the bias condition in active mode. (b) Energy band diagram around permeable metal base. $q\varphi_{BE}$ is the emitter-base Schottky barrier height, $q\varphi_B$ is the effective barrier height in the permeable region with respect to the Fermi level, and $q\varphi_{BC}$ is the collector-base Schottky barrier height. The green dash line describes the conduction band contour through the permeable region. (c) Cross-sectional Transmission-electron microscope view of Al(100nm)/C60(60 nm)/Al(10 nm)/Me-PTCDI(500 nm)/ITO. Inset is the magnified view of a permeable region showing direct emitter-collector contact in the permeable area.

2. Results and Discussion

2.1. Charge Transmission in PMBTs

Figure 1a shows the schematic device structure used in this work. The device has a semiconductor-metal-semiconductor structure which can be considered as a back-to-back Schottky diode.[4,25,26] In active mode, the emitter-base diode is under forward bias and the collector-base diode is under reverse bias. Carriers are transmitted from the emitter through the base to the collector. There are two kinds of charge transmission through the base layer. One is hot-electron transmission through the metallic base region, and the other is electron transmission through the permeable base region with the current path shown as the green dash line in Figure 1b. If

hot-electron transmission is the dominant process, the collector current density via hot-electron transport ($J_{c,h}$) is given by the following equation[26]:

$$J_{C,h} = \alpha_h J_E = \alpha_B \alpha_{BC} \alpha_C J_E \quad (1)$$

where α_h is charge transmission ratio via hot-electron transport, J_E is the emitter current density, α_B is electron scattering ratio in the base, α_{BC} is quantum-mechanical reflection of electrons at base-collector Schottky junction, and α_C is electron scattering due to the image force lowering of the base-collector junction barrier. J_E is given by[26]

$$J_E = T^2 \exp\left(\frac{q\phi_{BE}}{kT}\right)\left[\exp\left(\frac{qV_{BE}}{kT}\right) - 1\right] \quad (2)$$

where A^* is the Richardson-Schottky constant, T is absolute temperature, φ_{BE} is the emitter-base Schottky-barrier height, k is the Boltzmann constant, and V_{BE} is the emitter-base forward bias; α_B is given by[26]

$$\alpha_B = \exp(-w/\lambda_B) \quad (3)$$

where w is the thickness of the base and λ_B is the electron mean scattering path in the base; α_{BC} is given by[26]

$$\alpha_{BC} = 1 - \left[\left(1 - \sqrt{1 - \frac{q\phi_{BC}}{q\phi_{BE}}}\right) \Big/ \left(1 + \sqrt{1 - \frac{q\phi_{BC}}{q\phi_{BC}}}\right)\right]^2 \quad (4)$$

where $q\varphi_{BC}$ is the Schottky barrier at the base-collector junction; α_C is given by[26]

$$\alpha_C = \exp(-d/\lambda_C) \quad (5)$$

where d is the distance between the metal surface and the image-force lowered barrier and λ_C is the mean scattering path of electrons in the collector.

For hot-electron transmission, asymmetrical Schottky barriers are preferred because electrons from the emitter have a higher potential energy to be transmitted through the base. However, due to electron scattering and reflection in the metal base, the charge transmission ratios (J_C/J_E) is less than 0.5.[27] On the other hand, direct electron transmission from the emitter to the collector occurs through the permeable base region, and the electrons are not scattered within the metal base region. Accordingly, the collector current density via permeable base transport ($J_{C,p}$) is a function of the effective barrier height ($q\varphi_B$), and φ_B is controlled by a linear combination of V_{BE} and V_{BC}.[4]

$$J_{C,p} = f[V_{BE}, V_{BC}] \quad (6)$$

Hence, the total J_C in PMBT is described by,

$$J_C = J_{C,h} + J_{C,p} \quad (7)$$

If $J_{C,h} \geq J_{C,p}$, it is called hot-electron transistor, and if $J_{C,h} \leq J_{C,p}$, called permeable-base transistor.

2.2. Formation of Nano-Pores in Metal Base Films

Figure 1c presents the cross-sectional transmission electron microscopy (TEM) view of our device with a 10 nm-thick Al base. Me-PTCDI is known to yield a granular growth with an average grain size around one hundred nanometers.[17,28] A thin film of Al deposited on it tends to reproduce the granular morphology which also affects the subsequent growth of C_{60}. It should be noted that the mean peak-to-valley variation of the Me-PTCDI surface is about 20 nm, which is twice the base thickness. As a result, the resulting Al film does not cover the entire Me-PTCDI surface, leading to the formation of pores in the valley region (inset in Figure 1b). While Al wetting on Me-PTCDI may affect the pore formation, the geometrical factor here seems to be the dominant parameter determining the film porosity. The average pore size is estimated to be 20 nm, and direct contact between the emitter and the collector semiconductors is clearly observed in the pore area. While the pores are randomly distributed, the base continuity should be maintained in order for the metal layer to function as an electrode. To support the geometrical effect on the pore formation, we refer to the report by Zheng Xu et al. demonstrating a vertical organic light-emitting transistor by depositing a 17 nm-thick Al source electrode on the light-emitting polymer.[29] In spite of the thin Al film thickness, no pinholes were found due to the smooth polymer surface at the bottom.

2.3. Common-Base Measurements

2.3.1. Charge Transmission Behaviors

Figure 2a shows the common-base plots for devices with different base thicknesses. Al is used as the emitter electrode due to its low work function resulting in a low contact barrier height for electrons (Supplementary Figure S4). In the common-base configuration, the base is ground, the emitter current is fixed from 0.025 mA/cm^2 to 0.225 mA/cm^2 in steps of 0.05 mA/cm^2, and the collector voltage is swept from –2 V to 2 V. With a 10 nm-thick base, most of the emitter electrons are collected by the collector. The common-base gain (α) defined as I_C/I_E at V_{CB} = 0 V ($V_{CB} = V_C - V_B$) is 0.97, indicating that 97% of the charge carriers from the emitter transmit through the base. As the base film gets thicker, α gradually decreases. The V_{CB} required for attaining 100% charge transmission ($\alpha = 1$) shifts from 0.4 V for the device with a 10 nm-thick base to more than 2 V for the device with a 30 nm-thick base, indicating that a higher V_{CB} is required to attain the charge transmission as the base thickness increases. At a base thickness of 70 nm, pores are not present and carriers cannot transmit through the base electrode resulting in the low charge collection from the emitter.

2.3.2. Porosity Measurement

One way to gauge the natural porosity within the thin metal film is to measure the V_E dependence on V_C sweep in the common-base configuration. If V_{EB} is not affected by V_{CB} sweeping at a fixed emitter current ($\delta V_{EB}/\delta V_{CB} = 0$), the base metal layer is

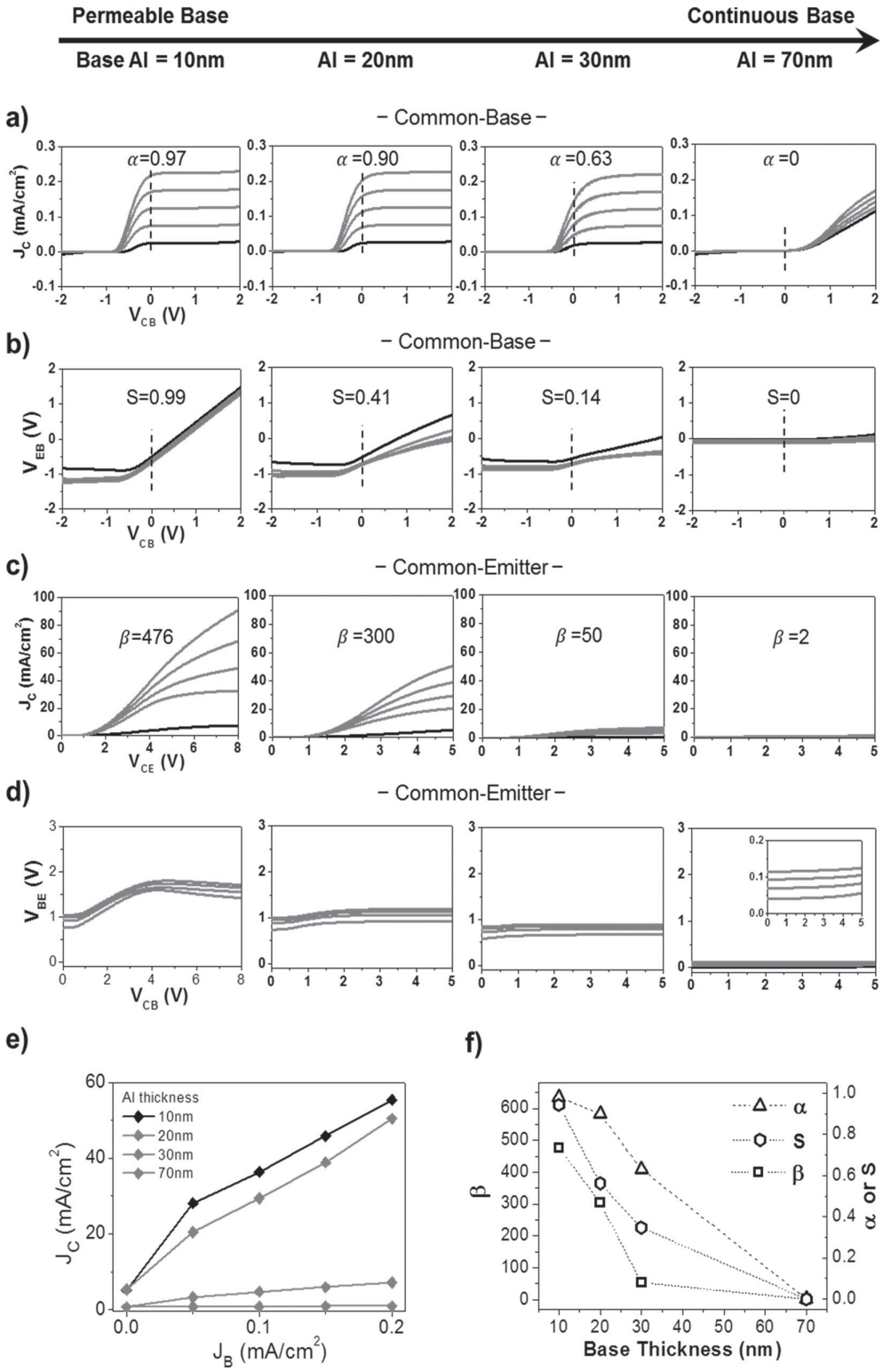

Figure 2. Common-base and common-emitter characteristics of devices as function of base thickness from 10 nm to 70 nm. (a) Common-base plots. I_E is applied from 0.025 mA/cm^2 to 0.225 mA/cm^2 in 0.05 mA/cm^2 step. $\alpha = I_C/I_E$ is calculated at $V_{CB} = 0$ V. (b) V_{EB} versus V_{CB} extracted from the common-base plots in Figure 2a. $S = \delta V_{EB}/\delta V_{CB}$ is the average slope of all curves at $V_{CB} = 0$ V. (c) Common-emitter plots. I_B is applied from 0 to 0.2 mA/cm^2 in 0.05 mA/cm^2 step. $\beta = [I_C\ (I_B = 0.05\ \text{mA/cm}^2) - I_C\ (I_B = 0)]/(I_B = 0.05\ \text{mA/cm}^2)$ at $V_{CE} = 5$ V. (d) V_{BE} versus V_{CE} for $I_B = 0.05 \sim 0.2$ mA/cm^2 extracted from the common-emitter plots in Figure 2c. (e) Collector current versus base current at $V_{CE} = 5$ V extracted from the common-emitter plots in Figure 2c. (f) Correlation between common-base gain (open triangles), voltage feedback between emitter and collector (open hexagons), and common-emitter gain (β, open squares) as function of base thickness.

regarded as continuous and electrically separating the emitter and the collector. If $\delta V_{EB}/\delta V_{CB} = 1$, on the other hand, it means the base is permeable through which there is a strong electric field coupling between the emitter part and the collector part. In fact, the values, 0 or 1, have been used to determine whether the device is a hot electron transistor ($\delta V_{EB}/\delta V_{CB} = 0$) or a permeable base transistor ($\delta V_{EB}/\delta V_{CB} = 1$).[26] However, if the variation of the pore size in our devices is on the order of a few tens of nanometers, the $\delta V_{EB}/\delta V_{CB}$ ratio can have values between 0 and 1 depending on the base thickness. Therefore, we exploit the range of the value to directly determine the degree of the porosity.

Figure 2b shows a plot of V_{EB} as a function of V_{CB} for the conditions described in Figure 2a. As the base thickness decreases from 70 nm to 10 nm, the voltage feedback (S) defined as the average slope of the curves at $V_{CB} = 0$ V increases from 0 to 1, meaning a gradual change from a continuous to permeable base, or in other words, evolution from a hot electron transistor to a permeable base transistor. The plateau region observed at $V_{CB} << -0.9$ V is coincident to the zero collector current region in Figure 2a. Here, all electrons injected from the emitter drain out to the base due to the potential barrier existing between the emitter terminal and the collector terminal. Accordingly, sweeping V_{CB} in this range does not affect the emitter-base current flow leading to a constant V_{EB} region. If $V_{CB} > -0.9$ V, on the other hand, the potential barrier becomes low enough to allow electron transmission through the permeable base region. Under V_{CB} sweeping, the barrier lowering at the pore region will result in a stronger electron injection from the emitter, necessitating the readjustment of V_{EB} to keep the emitter current constant. Hence, a higher base porosity leads to a larger change in V_{EB}, or in other words, larger degree of voltage feedback (S).

2.4. Common-Emitter Measurements

As a result of the increased porosity, collector current modulation by a base current is increased. Figure 2c shows the base current-controlled common-emitter plots for the same devices in Figure 2a and 2b. In the common-emitter configuration, the emitter is ground and the base current is fixed from 0 to 0.2 mA/cm^2 in steps of 0.05 mA/cm^2 while the collector voltage is swept from 0 to 5 V (in case of a 10 nm-thick base, the collector voltage is applied from 0 V to 8 V). For the device with a 70 nm-thick Al base, α is nearly zero and negligible collector current modulation was observed. As the base thickness becomes thinner, on the other hand, the collector current modulation efficiency is significantly enhanced. The common-emitter gain (β) or current amplification factor defined as $\Delta I_C/\Delta I_B$ at $V_{CE} = 5$ V increases from 2 for the 70 nm-thick base device to 476 for the 10 nm-thick base device with output collector current saturation. To our knowledge, this is the highest reported current gain to date. As observed in Figure 2e, all devices in Figure 2c shows nearly a linear relationship between the base current and the collector current where the current gain presented as the slope gradually increases with decreasing the Al film thickness. Figure 2d plots the V_{BE} versus V_{CE} for the common-emitter curves in Figure 2c. Unlike the base voltage-controlled devices reported by previous authors[16–18] where the fixed base voltage did not fix the base current, our device shows nearly constant base voltage in the collector current saturation region under a fixed base current. As observed, the V_{BE} values to fix the base currents from 0.05 to 0.2 mA/cm^2 gradually decrease as Al film thickness is increased. This is because the porous Al region is decreased as Al film gets thicker, resulting in more electron injection into the metal base regions. Accordingly, less V_{BE} is required to generate a fixed base current. Figure 2e summarizes the effect of the base film thickness on α, β, and S. As expected, the device parameters and hence the device performance are strong functions of the base thickness.

2.5. Surface Morphology of Metal Base Films and the Porosity Calculation

In addition to the voltage feedback analysis, atomic force microscopy (AFM) was used to quantify the metal base porosity. In the height topography mode, it is not sufficient to observe the contrast in surface heterogeneity to identify the presence of pores in the metal base. In the phase image mode, on the other hand, the contrast is sufficient to differentiate the exposed Me-PTCDI region through the pores from Al regions. **Figure 3**a-d represents the 3D phase images of the Al base surfaces with thicknesses from 10 nm to 70 nm on top of a 500 nm-thick Me-PTCDI film. With a 10 nm-thick Al film, the high phase contrast (RMS roughness = 16°) indicates that a high density of

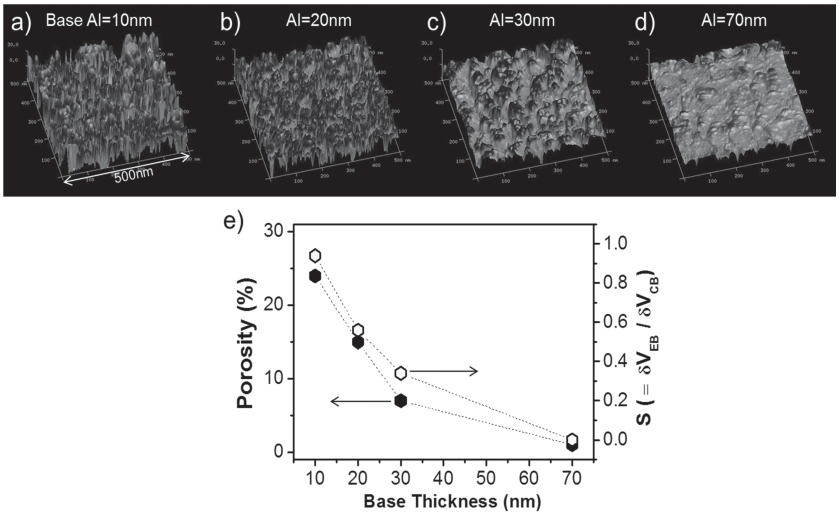

Figure 3. (a)-(d) Surface phase images of Al base film with different thickness. The samples are Al(10 nm~70 nm)/Me-PTCDI(500 nm)/ITO. The scan size and the phase scale are same for all images as 500 nm x 500 nm and 60° respectively. (e) Correlation between the porosity and the voltage feedback value. Here, the voltage feedback data in Figure 2f is used again for comparison.

pores presents on the surface. As the base thickness increases to 70 nm, the phase becomes homogeneous (RMS roughness = 4°) revealing almost a complete Al coverage on the Me-PTCDI surface. The porosity was calculated by dividing the number of image pixels in the porous area by the number of pixels in the investigated area (the details are in the Supplementary Figure S5). As observed in Figure 3e, the calculated porosity varies from 24% for the 10 nm-thick base device to 1% for the 70 nm-thick base device, which is closely correlated with the voltage feedback value (S).

2.6. Effect of Emitter-Collector Thickness Ratio on Device Operation Window

In order to understand the device physics further, the effect of Me-PTCDI thickness was examined. If Me-PTCDI thickness is reduced, higher electric field in the collector layer will cause a larger base-to-collector electron flow under device operation. **Figure 4** demonstrates a series of common-base plots with different Me-PTCDI thickness. As observed in Figure 4a, base-to-collector electron flow increases at around V_{CB} = 1V by decreasing the Me-PTCDI thickness from 500 nm to 100 nm, resulting in $I_C > I_E$. In fact, the collector current saturation region in the common-base plots is the ideal PMBT operation window because common-base gain is nearly 1 in the region. Due to the increase of the electron injection from base to collector, the window becomes narrower with decreasing the collector layer thickness. If Me-PTCDI is used as emitter, on the other hand, a reverse trend occurs. Now, 500 nm-thick emitter layer is too thick to efficiently emit electron from ITO. Rather, the higher electric field in the C_{60} collector causes a high base-to-collector electron flow leading to the narrow operation window in the common-base plot for Me-PTCDI = 500 nm case in Figure 4b. As the Me-PTCDI emitter thickness decreases from 500 nm to 100 nm, more efficient charge injection from ITO results in the enhanced collector current modulation at lower V_{CE} as observed in the corresponding common-emitter plots. It is interesting that base-to-collector electron flow in the common-base plots in Figure 4b is decreased in spite of the

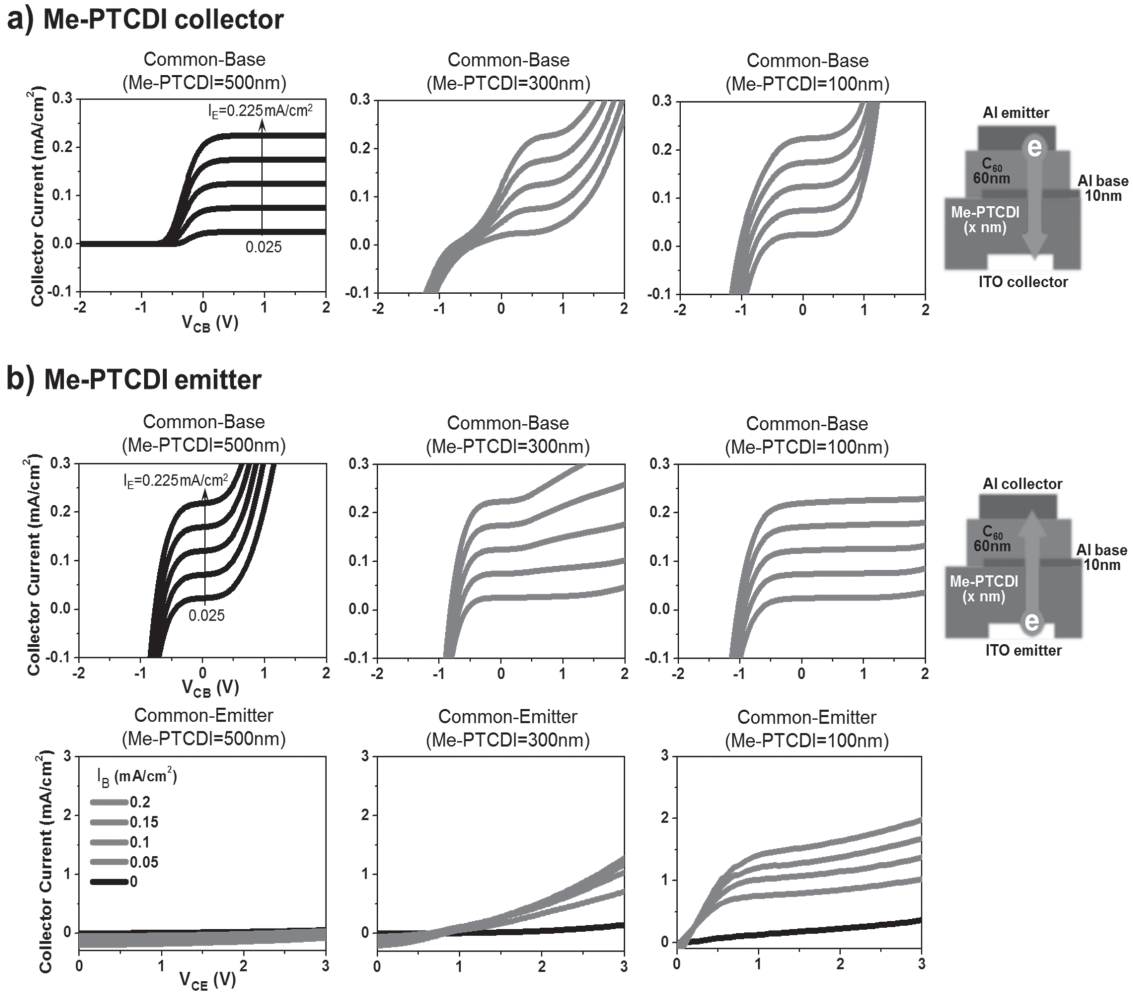

Figure 4. Effect of Me-PTCDI thickness on device operation window. The schematic device structures are illustrated on the right side. Me-PTCDI is used as either collector or emitter by reversing the bias condition. (a) Common-base plots of the devices with different Me-PTCDI thickness when used as the collector layer. I_E is applied from 0.025 to 0.225 mA/cm^2 in 0.05 mA/cm^2 steps in all the three plots. (b) Common-base and common-emitter plots when Me-PTCDI is used as the emitter layer.

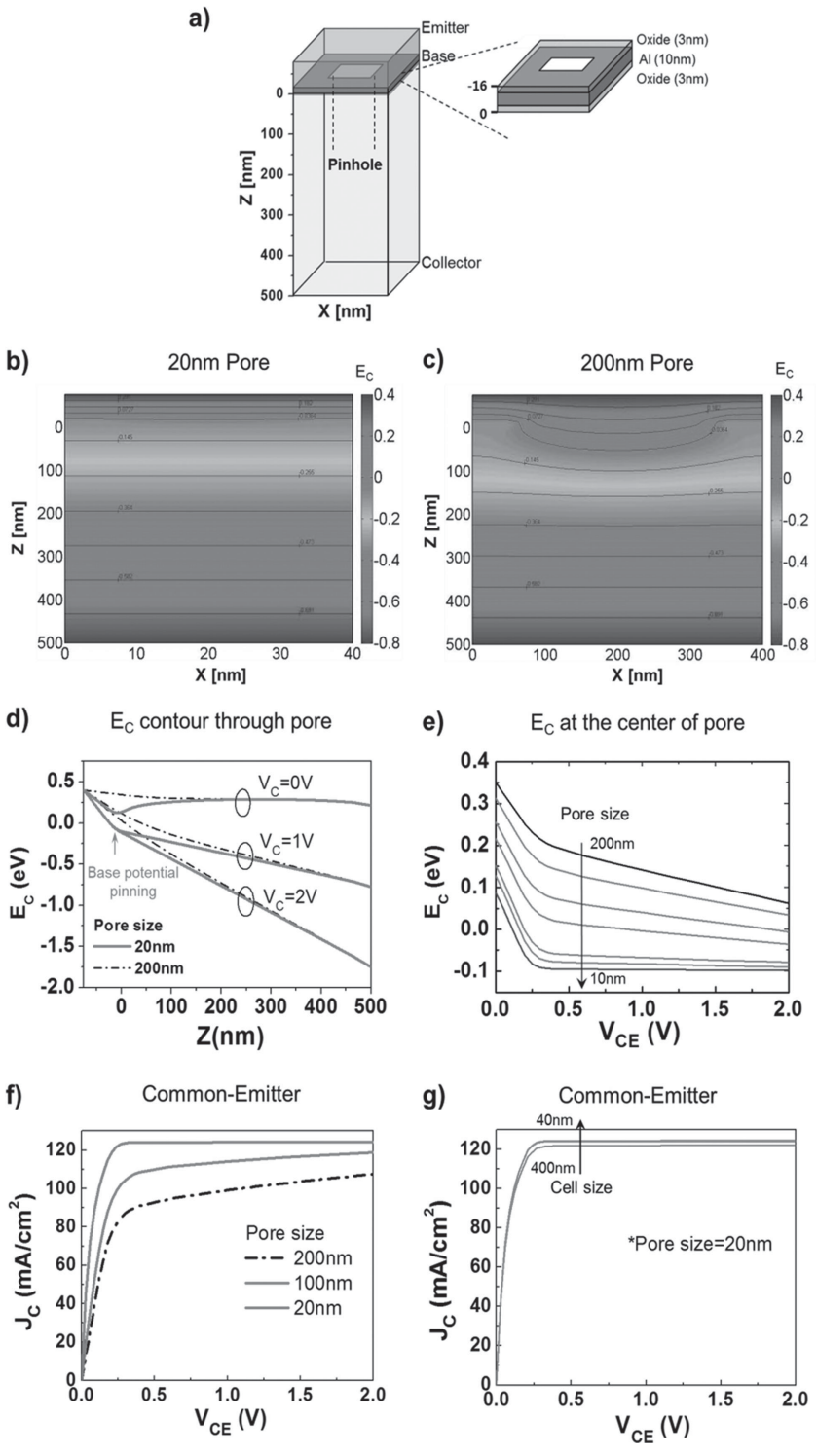

Figure 5. (a) Simulated device structure. Square-shaped pore and 3 nm-thick oxide around base are assumed. More details are in the supplementary section. (b) Conduction band profile of X-Z plane cutting at the middle of *y*-axis for 20 nm × 20 nm pore in 40 nm × 40 nm Al base and (c) 200 nm × 200 nm pore in 400 nm × 400 nm Al base. V_E, V_B, and V_C are fixed at 0, 0.5, and 1 V respectively for both cases. (d) Conduction band contours from the emitter to the collector through the center of the pore. V_C is varied from 0 to 2 V in 1 V steps. The potential for 20 nm-sized pore is pinned when $V_{CE} > 1$V. (e) Conduction band energy at the center of the pore region with different pore size between 10 nm and 200 nm. The cell size is varied for the porosity to be kept at 50% in all conditions. (f) Common-emitter characteristic of simulated device with different pore size and same porosity. (g) Common-emitter characteristic of simulated device with same pore size and different pore density (cell size: 40 nm, 100 nm, and 400 nm). For (d)-(g), V_E and V_B are kept constant as 0V and 0.5V respectively.

same C_{60} collector layer thickness, resulting in almost no base-to-collector electron leakage for Me-PTCDI = 100 nm device. We believe that due to the electric field coupling between the emitter layer and the collector layer through the porous Al base, relative ratio of emitter thickness to collector thickness becomes more important for device operation than the absolute thickness. As far as the material for each layer is chosen, smaller thickness ratio of emitter layer to collector layer is better for larger device operation window, as observed in the two reverse cases.

2.7. Determination of Dominant Charge Transmission Mechanism

As explained, in our device there exist only two current paths consisting of C_{60}/Me-PTCDI through permeable base region and C_{60}/Al/Me-PTCDI through the metal base regions. In order to determine the dominant charge transport mechanism, hot-electron transmission equation was used. In the three scattering factors explained in Equations (3)–(5), quantum-mechanical reflection (4) and scattering due to the image-force lowering (5) are dependent on choice of materials whereas electron scattering in the base (3) is dependent on the thickness of the base layer. Accordingly, if changing the base thickness leads to an exponential variation of J_C under a fixed J_E and bias conditions, hot electron transmission should be the dominant charge transmission mechanism. Based on the common-base plots of our devices in Figure 2a, changing Al base thickness from 10 nm to 70 nm does not lead to an exponential variation of common-base gain (α) value at any V_{CB} region. Therefore, hot electron transmission is not the dominant charge transmission mechanism. On the other hand, if permeable base transmission is dominant, the charge transmission in two reverse directions can reach 100% (α = 1) in common-base measurement because the barrier height ($q\varphi_B$) in the permeable region is controllable by the linear combination of the collector bias and the emitter bias. When comparing the common-base plot for

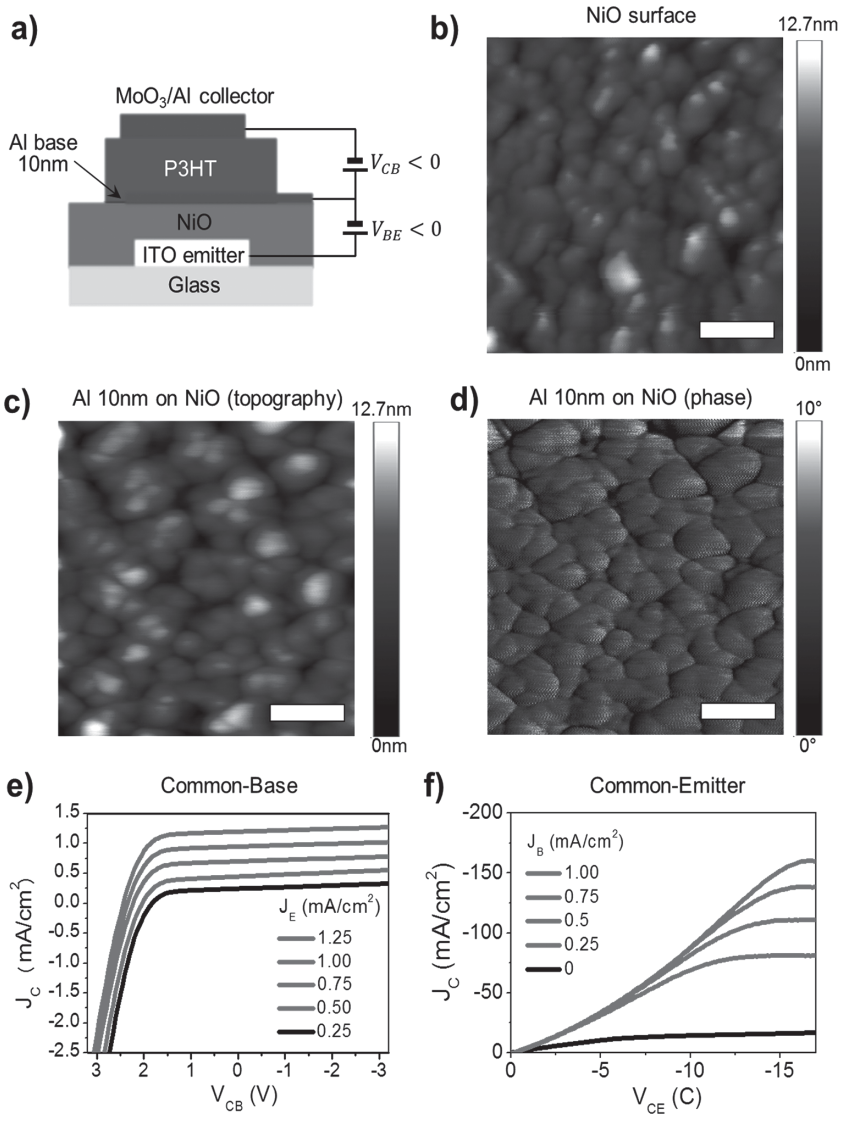

Figure 6. (a) Structure of inorganic PMBT using solution-processed NiO and P3HT as emitter and collector semiconductors respectively. In active mode, forward bias is applied at NiO-Al junction ($V_{BE} < 0$) and reverse bias at Al-P3HT junction ($V_{CB} < 0$). AFM topography images of (b) solution-processed NiO surface and (c) 10 nm-thick Al layer deposited on top of the NiO layer. (d) AFM phase image of Figure 5c. All scale bars in the images in (b), (c), and (d) are 50 nm. (e) Common-base plot of inorganic PMBT. The base is ground, the emitter current is applied from 0.25 to 1.25 mA/cm^2 in steps of 0.25 mA/cm^2, and V_{CB} is swept from +3 to −3 V. (f) Common-emitter plot. The emitter is ground, the base current is applied from 0 to 1 mA/cm^2 in steps of 0.25 mA/cm^2, and V_{CE} is swept from 0 to −17 V.

500 nm-thick Me-PTCDI in Figure 4a with that in Figure 4b, the charge transmission ratio (α) in the saturated collector current region (at $V_{CB} = 1$ V for 4a and $V_{CB} = 0$ V for 4b) reaches almost 1 ($I_E \approx I_C$) in both directions. Therefore, the dominant charge transmission mechanism in our device is permeable base transmission.

2.8. Device Simulation: Effect of Pore Size and Pore Density

When controlling the Al base film thickness, the pore size and density are changing at the same time. In order to separate the two factors and examine the current saturation mechanism, three-dimensional (3D) device simulation was performed. **Figure 5**a illustrates the schematic diagram of the modeled device structure which shows the base region is surrounded by an insulator layer of aluminum oxide. A periodic boundary condition is used in the horizontal directions so that a periodic array of pores is simulated. Details of the device simulation are provided in the Supplementary Section. Figures 5b and 5c are the potential profiles in the x–z plane cutting through the center of the 20 nm × 20 nm pore in a 40 nm × 40 nm base cell and the center of the 200 nm × 200 nm pore in a 400 nm × 400 nm base cell. Note that the porosity is the same for both cases. For simplicity, a square-shaped pore is used in this simulation. It should be noted that the exact geometry of the pore has a minimal effect on the simulation results. The potential around the pores is more sensitive to the changes in the collector bias for a large pore device (LPD) compared to a small pore device (SPD). Figure 5d shows the potential profiles of the two devices through the center of the pore along z direction for different collector bias voltages with a fixed base voltage. For a SPD, the potential in the pore region is more sensitive to the base bias. At high collector biases, the potential at the base is pinned by the base bias regardless of the collector bias. Hence, the electric field in the emitter region is also pinned as shown in Figure 5d, and the emitter current is constant regardless of the collector bias, leading to the collector current saturation. On the other hand, there is no potential pinning at the base for LPD, resulting in no current saturation. Figure 5e describes the conduction band energy at the center of the pore region as a function of a collector bias for different pore sizes. As the pore size decreases from 200 nm to 10 nm, the potential pinning effect at the center of the pore region becomes more prominent. The potential pinning effect is due to the electrostatic effect by both the base electrode and the collector electrode. If the pore size is small compared to the collector layer thickness, the electrostatic potential in the pore is pinned by the base bias. On the other hand, if the pore size is large, the collector bias will have more dominant effect on the electrostatic potential in the pore region. Figure 5f shows the common-emitter characteristics with different pore sizes varying from 200 nm to 20 nm while keeping the porosity unchanged. As expected from Figure 5e, the device with 20 nm-sized pore shows a strong current saturation compared to the device with 200 nm-sized pore. On the other

hand, Figure 5g demonstrates the common-emitter characteristic for the same pore size and different pore density by varying the cell size. As clearly shown, current saturation was observed regardless of the different pore density due to the effect of the small pore size. Therefore, we conclude that the potential pinning effect in the small pore size observed in our device is the dominant parameter for the current saturation rather than the pore density.

2.9. Fabrication of Solution-Processed Nickel Oxide PMBT

Based on understanding of the device physics, we also fabricated a p-type organic-inorganic hybrid PMBT using a solution-processed NiO emitter layer and a solution-processed P3HT collector layer. In **Figure 6**a, the schematic device structure is described in active mode. The detailed fabrication is described in the method section. Figure 6b presents the topography image of the solution-processed NiO surface with 20~30 nm grains. Deposition of a 10 nm-thick Al base film on top of the NiO surface reproduces the granular morphology (Figure 6c). Figure 6d presents the phase image of Figure 6c. As seen in the figure, the phase contrast indicates the presence of 20~30 nm Al grains, which reveals the natural pore formation on the NiO surface (Figure 6d). As a result of this, the average common-base gain (α) reaches 0.94 at $V_{CB} = 0$ V and nearly 1 at $V_{CB} = -2$ V (Figure 6e). Also, a high common-emitter current gain (β) of 260 can be achieved at $V_{CE} = -15$ V with apparent collector current saturation (Figure 6f).

3. Conclusions

In conclusion, we have fabricated organic n-type PMBTs by controlling the thickness of the thin metal base film on top of an organic semiconductor with a granular surface. By controlling the metal base porosity, we could achieve a maximum common-emitter current gain of 476 with output current saturation. Quantification of the metal base porosity indicates that the device performance is strong function of the natural porosity. From the results of the device simulation, we attribute the current saturation mechanism to the potential-pinning effect in the small pore region. In addition to the n-type organic PMBT, we also demonstrated NiO-based p-type PMBTs with high common-emitter current gain of 260 and output current saturation. Our approach to fabricate and characterize the high gain PMBTs will contribute to the understanding of the fundamental physics and realization of truly high-performance organic and inorganic PMBTs for a high gain current amplifier.

4. Experimental Section

Fabrication of organic PMBTs: Each layer of the device was thermally evaporated using shadow masks at a pressure of 10^{-6} Torr. ITO-coated glass substrates were ultra-sonicated in acetone and then isopropanol for 15 minutes respectively. Next, the substrates were UV-ozone treated for 15 minutes using a UV-ozone cleaner. A 500 nm-thick Me-PTCDI (N,N′-dimethyl-3,4,9,10-perylene tetracarboxylicdiimide, Luminescence Technology Corp.) film was evaporated on the UV-ozone treated ITO substrate at a rate of 0.2 nm/s. Then, a 5–70 nm-thick Al film was deposited at 0.2 nm/s. The samples were then taken out to the ambient and heat-treated on a hot plate at 150 °C for 1 hour. After annealing, the samples were moved back to the vacuum chamber and subsequently a 60 nm-thick C_{60} film (Materials and Electrochemical Research Corp.) was deposited on top of the substrate at a rate of 0.1 nm/s. For the emitter electrode, 100 nm-thick Al or a 30 nm-thick Ag were deposited at 0.01 nm/s and 0.2 nm/s respectively. The active area is 4 mm^2 defined by the overlap region between the emitter, base, and collector electrodes. To wire out the highly resistive thin Al base film, Ag paste is covered on top of the base electrode as close to the active area as possible. Thickness was monitored by quartz microbalance and confirmed by a Dektak 150 profilometer.

Fabrication of NiO-based PMBT: For the fabrication of nickel oxide (NiO)-based PMBT, we used sol-gel derived NiO with nickel acetate dihyrate and ethanolamine as the precursors in ethanol and the procedures were documented in our previous publication.[30] On top of the NiO film, 10 nm-thick aluminum base electrode was evaporated, followed by spin-coating a 5 wt.% poly(3-hexylthiophene) (P3HT) collector layer. To suppress the leakage current we evaporated insulating lithium fluoride (LiF) layers above and below the Al base film. Finally 5 and 50 nm-thick molybdenum oxide (MoO_3) thick films and an Al collector electrode were evaporated.

Device characterization: Electrical performance of the device was measured in the air without encapsulation using Keithley 4200-SCS parameter analyzer. Throughout this work, V_{AB} represents $V_A - V_B$. Samples for transmission electron microscopy analysis were prepared by focused ion beam and measured using JEOL 2010F operated at 200 kV. Atomic force microscopy (AFM Dimension 3100, tapping mode) and Kelvin probe force microscopy (Bruker Corp.) measurements were performed in air. Porosity was calculated using Photoshop. Details for X-ray photo-emission spectroscopy (PHI5000 Versa Probe II) measurement, Kelvin-probe force microscopy (Bruker Corp.) measurement, and device simulation are in the supplementary section.

Supporting Information

Supporting Information is available from the Wiley Online Library or from the author.

Acknowledgements

H. Y., J. H. K. and F. S. acknowledge the support of this work by Wintek Corporation.

Received: February 24, 2014
Revised: May 13, 2014
Published online: July 22, 2014

[1] A. J. Heeger, D. J. Heeger, J. Langan, Y. Yang, *Science* **1995**, *270*, 1642–1644.
[2] Y. Yang, A. J. Heeger, *Nature* **1994**, *372*, 344–346.
[3] S. S. Cheng, Y. C. Chuang, D. Kekuda, C. W. Ou, M. C. Wu, C. W. Chu, *Adv. Mater.* **2009**, *21*, 1860.
[4] T. Yajima, Y. Hikita, H. Y. Hwang, *Nat. Mater.* **2011**, *10*, 198–201.
[5] J. P. M. Serbena, I. A. Hummelgen, T. Hadizad, Z. Y. Wang, *Small* **2006**, *2*, 372–374.
[6] K. Fujimoto, T. Hiroi, K. Kudo, M. Nakamura, *Adv. Mater.* **2007**, *19*, 525.
[7] Y. C. Chao, M. C. Niu, H. W. Zan, H. F. Meng, M. C. Ku, *Org. Electron.* **2011**, *12*, 78–82.
[8] C. O. Bozler, *Surf. Sci.* **1986**, *174*, 487–500.

[9] M. S. Meruvia, I. A. Hummelgen, M. L. Sartorelli, A. A. Pasa, W. Schwarzacher, *Appl. Phys. Lett.* **2004**, *84*, 3978–3980.
[10] M. S. Meruvia, A. R. V. Benvenho, I. A. Hummelgen, A. A. Pasa, W. Schwarzacher, *Appl. Phys. Lett.* **2005**, *86*.
[11] C. G. Feng, M. D. Yi, S. Y. Yu, D. G. Ma, *Appl. Phys. Lett.* **2006**, *88*.
[12] J. Y. Huang, M. D. Yi, I. A. Hummelgen, D. G. Ma, *Org. Electron.* **2009**, *10*, 210–213.
[13] M. D. Yi, S. Y. Yu, C. G. Feng, T. Zhang, D. G. Ma, M. S. Meruvia, I. A. Hummelgen, *Org. Electron.* **2007**, *8*, 311–316.
[14] M. D. Yi, J. Y. Huang, D. Ma, I. A. Hummelgen, *Org. Electron.* **2008**, *9*, 539–544.
[15] K. Zhao, J. C. Deng, X. M. Wu, X. M. Cheng, J. Wei, S. G. Yin, *Org. Electron.* **2011**, *12*, 1003–1009.
[16] K. Nakayama, S. Fujimoto, M. Yokoyama, *Appl. Phys. Lett.* **2006**, *88*.
[17] S. Fujimoto, K. Nakayama, M. Yokoyama, *Appl. Phys. Lett.* **2005**, *87*.
[18] Y. C. Chao, H. F. Meng, S. F. Horng, C. S. Hsu, *Org. Electron.* **2008**, *9*, 310–316.
[19] S. S. Cheng, C. Y. Yang, Y. C. Chuang, C. W. Ou, M. C. Wu, S. Y. Lin, Y. J. Chan, *Appl. Phys. Lett.* **2007**, *90*.
[20] T. M. Ou, S. S. Cheng, C. Y. Huang, M. C. Wu, I. M. Chan, S. Y. Lin, Y. J. Chan, *Appl. Phys. Lett.* **2006**, *89*.
[21] C. Y. Yang, T. M. Ou, S. S. Cheng, M. C. Wu, S. Y. Lin, *Appl. Phys. Lett.* **2006**, *89*.
[22] S. S. Cheng, J. H. Chen, G. Y. Chen, D. Kekuda, M. C. Wu, C. W. Chu, *Org. Electron.* **2009**, *10*, 1636–1640.
[23] J. P. M. Serbena, J. Y. Huang, D. Ma, Z. Y. Wang, I. A. Hummelgen, *Org. Electron.* **2009**, *10*, 357–362.
[24] Y. C. Chao, M. H. Xie, M. Z. Dai, H. F. Meng, S. F. Horng, C. S. Hsu, *Appl. Phys. Lett.* **2008**, *92*.
[25] Simon. M. Sze, Kwok. K. Ng, *Physics of Semiconductor Devices* 3rd edn. John Wiley **2007**.
[26] M. S. Meruvia, I. A. Hummelgen, *Adv. Funct. Mater.* **2006**, *16*, 459–467.
[27] S. M. Sze, C. R. Crowell, G. P. Carey, E. E. Labate, *J. Appl. Phys.* **1966**, *37*, 2690-&.
[28] A. Fischer, P. Siebeneicher, H. Kleemann, K. Leo, B. Lussem, *J. Appl. Phys.* **2012**, *111*.
[29] Z. Xu, S. H. Li, L. Ma, G. Li, Y. Yang, *Appl. Phys. Lett.* **2007**, *91*.
[30] J. R. Manders, S. W. Tsang, M. J. Hartel, T. H. Lai, S. Chen, C. M. Amb, J. R. Reynolds, F. So, *Adv. Funct. Mater.* **2013**, *23*, 2993–3001.